nature biotechnology

High-throughput measurement of single-cell growth rates using serial microfluidic mass sensor arrays

Nathan Cermak[1,12], Selim Olcum[2,12], Francisco Feijó Delgado[2,3], Steven C Wasserman[3], Kristofor R Payer[4], Mark A Murakami[5], Scott M Knudsen[3], Robert J Kimmerling[3], Mark M Stevens[6], Yuki Kikuchi[4,11], Arzu Sandikci[2], Masaaki Ogawa[7], Vincent Agache[8], François Baléras[8], David M Weinstock[5,9] & Scott R Manalis[1–4,10]

Methods to rapidly assess cell growth would be useful for many applications, including drug susceptibility testing, but current technologies have limited sensitivity or throughput. Here we present an approach to precisely and rapidly measure growth rates of many individual cells simultaneously. We flow cells in suspension through a microfluidic channel with 10–12 resonant mass sensors distributed along its length, weighing each cell repeatedly over the 4–20 min it spends in the channel. Because multiple cells traverse the channel at the same time, we obtain growth rates for >60 cells/h with a resolution of 0.2 pg/h for mammalian cells and 0.02 pg/h for bacteria. We measure the growth of single lymphocytic cells, mouse and human T cells, primary human leukemia cells, yeast, *Escherichia coli* and *Enterococcus faecalis*. Our system reveals subpopulations of cells with divergent growth kinetics and enables assessment of cellular responses to antibiotics and antimicrobial peptides within minutes.

Single cells vary widely in their growth rates, a fundamental phenotype that reflects biochemical and biophysical differences between cells and may govern their relative abundance within a population. From bacteria to unicellular eukaryotes to metazoan cells, even genetically identical cells may grow at different rates owing to a combination of intrinsic molecular noise and various deterministic behavioral programs[1–5]. This variation is not observable via population-based growth assays but has important consequences for human health. For example, cancer cells within an individual may vary drastically in proliferative potential, with subsets capable of continuous cycling and others primarily arrested[6]. Similarly, growth-rate variation in bacterial populations can dictate the efficacy of antibiotic treatments, as slow- or nongrowing cells tend to be more resistant to antibiotics[7–9]. Despite its importance, precise and rapid quantification of single-cell growth rates remains technically challenging. One approach is to measure a cell's outline in a microscopic image and calculate its volume on the basis of assumptions about its three-dimensional shape—e.g., measuring the length of rod-shaped bacteria and assuming the cross-section stays constant[9–12] or measuring yeast cell boundaries and assuming the cell is a prolate ellipsoid[13]. However, it is not clear how often these shape assumptions are violated, and these methods are generally not usable for irregularly shaped cells. Another approach, quantitative phase microscopy, can be used to estimate a cell's dry mass over time[14,15] but, like other available platforms, it cannot perform precise, single-cell growth measurements on a variety of samples with high temporal resolution.

Recently, inertial methods for measuring single-cell growth have been developed on the basis of resonating micromechanical structures[16–18], some of which provide much higher precision than microscopy but are hindered by low throughput. These methods exploit the fact that a micromechanical resonator's natural frequency depends on its mass. Adding cells to a resonator alters the resonator's mass and causes a measurable change in resonant frequency. One such class of resonator mass sensor is the suspended microchannel resonator (SMR), which consists of a sealed microfluidic channel that runs through the interior of a cantilever resonator. The cantilever itself is housed in an on-chip vacuum cavity, reducing damping and improving frequency (and thus mass) resolution[19]. As a cell in suspension flows through the interior of the cantilever, it transiently changes the cantilever's resonant frequency in proportion to the cell's buoyant mass (the mass of the cell minus the mass of the fluid it displaces). In water, a cell's buoyant mass is roughly proportional to (and is typically about one-quarter of) its dry mass[20]. SMRs are very precise, weighing single mammalian cells with a resolution of 0.05 pg (0.1% of a cell's buoyant mass) or better[15–17]. It is possible to measure a cell's growth rate by repeatedly flowing the cell back and forth through the SMR cantilever, but this method is limited to one cell at a time. This limitation in throughput has prevented wider application of SMRs across a range of biological and clinical efforts.

Here we introduce an SMR-based technique that enables high-throughput growth-rate measurement while retaining the precision of the SMR. We use an array of SMRs fluidically connected in series

[1]Program in Computational and Systems Biology, Massachusetts Institute of Technology, Cambridge, Massachusetts, USA. [2]Koch Institute for Integrative Cancer Research, Massachusetts Institute of Technology, Cambridge, Massachusetts, USA. [3]Department of Biological Engineering, Massachusetts Institute of Technology, Cambridge, Massachusetts, USA. [4]Microsystems Technology Laboratories, Massachusetts Institute of Technology, Cambridge, Massachusetts, USA. [5]Department of Medical Oncology, Dana-Farber Cancer Institute, Harvard Medical School, Boston, Massachusetts, USA. [6]Department of Biology, Massachusetts Institute of Technology, Cambridge, Massachusetts, USA. [7]Innovative Micro Technology, Goleta, California, USA. [8]CEA-LETI, Minatec Campus, Grenoble, France. [9]Broad Institute, Cambridge, Massachusetts, USA. [10]Department of Mechanical Engineering, Massachusetts Institute of Technology, Cambridge, Massachusetts, USA. [11]Present address: Hitachi High-Technologies Corporation, Ibaraki-ken, Japan. [12]These authors contributed equally to this work. Correspondence should be addressed to S.R.M. (srm@mit.edu).

Received 3 November 2015; accepted 10 August 2016; published online 5 September 2016; doi:10.1038/nbt.3666

and separated by 'delay' channels (**Fig. 1a**,**b**). These delay channels give the cell time to grow as it flows between cantilevers. After a cell exits a cantilever, other cells are free to enter it and be weighed. As a result, we are not limited to flowing only one cell through the array at a time but can have many cells flowing in a queue. This enables high-throughput precision growth measurements across a wide array of suspended cell types. Here we demonstrate a proof-of-concept serial SMR array and show that it can measure lymphoid cell lines, primary mouse T cells, primary human lymphocytes and acute myeloid leukemia cells, *Saccharomyces cerevisiae*, *E. coli* and *E. faecalis*. We demonstrate previously unrecognized variability in growth kinetics and perform ultra-rapid assessment of susceptibility to antibiotics and antimicrobial peptides.

RESULTS

Device design

Before designing the serial SMR arrays, we first considered how the number of buoyant mass measurements (k), measurement resolution (σ_{mass}) and the time between measurements (Δt) affect the resolution of the mass accumulation rate. We derived a simple relationship for the standard error (resolution) of the mass accumulation rate in terms of these three quantities:

$$\sigma_{\text{mass accumulation rate}} \approx \frac{\sigma_{\text{mass}}\sqrt{12}}{k^{1.5}\Delta t} \quad (1)$$

(see **Supplementary Note 1** for derivation).

For serial SMR arrays, Δt can be controlled by adjusting the flow rate. Therefore, apart from guiding our designs, equation (1) also illustrates that we can easily tune the device's behavior to trade throughput for resolution by changing the flow rate; i.e., faster flow yields higher throughput but poorer resolution, and vice versa for slower flow (**Supplementary Note 1**).

In this work, we designed and validated two serial SMR arrays with different channel dimensions—one for larger cells (mammalian cells and yeast, 15 × 20 μm in cross-section) and one for bacteria (3 × 5 μm). Despite the differences in scale, the operation and design concepts for these devices are essentially identical.

For studying mammalian and yeast cells, which often accumulate mass at rates of 1–10 pg/h (ref. 16), we sought a mass accumulation rate resolution of <1 pg/h. Using the expected mass noise (σ_{mass} ~0.05 pg for similar single-SMR devices), we designed a device consisting of 12 SMRs fluidically connected in series by delay channels ~50 mm long (**Fig. 1b**). At typical SMR flow rates, Δt would be about 1.5 min, and the expected mass accumulation rate resolution would thus be 0.17 pg/h, resulting in a relative precision of 1–10%. We designed our small-channel devices similarly, but with 10 cantilevers and with the expectation of operating at faster flow rates (Δt ~30 s between SMRs).

To obtain the best possible mass resolution (σ_{mass}), we excited cantilevers in the second bending mode (**Fig. 1c**) so that the measured mass would not depend on the cell's flow path[21], thus avoiding a fundamental source of error for SMRs operated in the first mode. However, because the second mode is at a higher frequency, and the tip follows an arc with a shorter radius than in the first mode, cells often became trapped at the cantilever tip owing to centrifugal force[22,23]. This problem was exacerbated at the low flow rates (and therefore reduced drag forces) necessary for sufficient delay time between cantilevers. To overcome the trapping problem, we shortened the interior channel to extend only as far as the vibration node, where the centrifugal force is minimal (**Fig. 1c**).

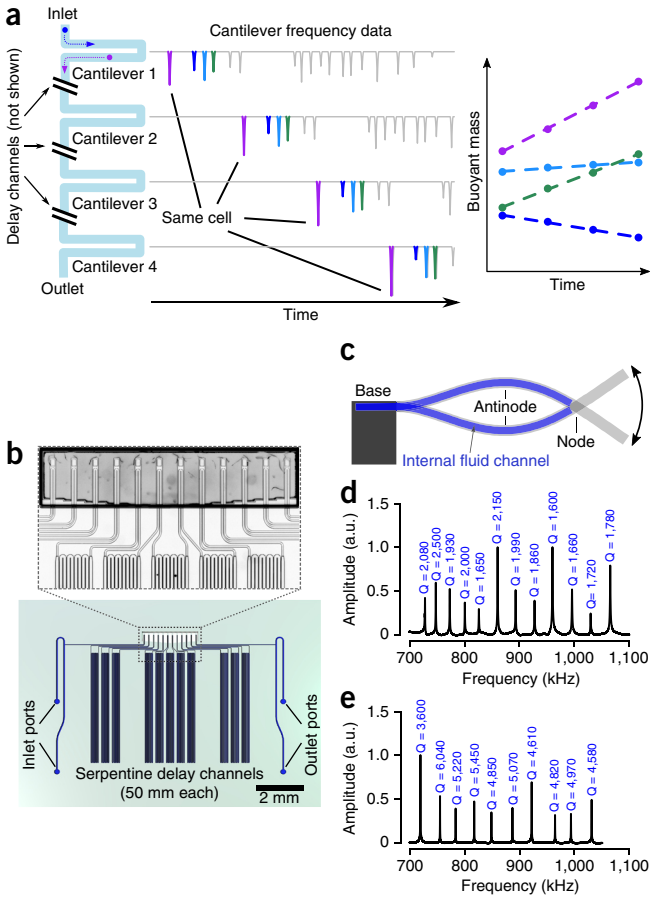

Figure 1 Design and implementation of the serial SMR array. (**a**) Simulated data showing frequency peaks originating from single cells flowing through a series of SMRs (cantilever mass sensors) separated by delay channels. Cells grow as they traverse the array. After frequency peaks originating from the same cell are grouped, that cell's mass accumulation rate can be obtained by regressing its buoyant mass versus time. Because many cells can traverse the array simultaneously, this device can achieve much higher throughput than a single SMR device. (**b**) Rendering of a large-channel serial SMR array device showing delay channels and the cantilevers (magnified in inset micrograph). (**c**) Side-view illustration of an SMR vibrating in the second bending mode. To prevent cells from getting trapped at the end of the cantilever by large centrifugal forces, the internal microfluidic channel (blue) extends only to the node of the second eigenmode. (**d**) Transfer function amplitude measured a large-channel serial SMR array, demonstrating frequency spacing of approximately 30 kHz and typical quality factors of 1,500–2,500. (**e**) Transfer function for a small-channel serial SMR array. a.u., arbitrary units.

So that each cantilever could be operated individually without coupling or interacting with other cantilevers, we used frequency-division multiplexing. We designed each cantilever with a unique resonant frequency roughly 30 kHz apart from that of its neighbors (**Fig. 1d**,**e**), which we controlled by varying cantilever lengths from 380 to 470 μm (large-channel devices) or from 180 to 215 μm (small-channel devices). This frequency spacing is conservative, as we estimate on the basis of Carson's rule[24] that the spacing could be reduced to less than 1 kHz in future devices, enabling operation of hundreds of cantilevers simultaneously within the frequency band used here (700–1,100 kHz).

Device operation and data analysis

To simultaneously measure the resonant frequency of all k cantilevers in the array, we first needed to measure the superposition of all the

cantilever deflection signals. We employed two approaches: (i) an optical lever setup, in which all cantilevers are simultaneously illuminated and a single photodetector measures the superposition of their deflection signals (**Supplementary Fig. 1**), or (ii) using devices with piezoresistors doped into the base of each cantilever[22,25], which are wired in parallel and their combined resistance measured via a Wheatstone bridge–based amplifier. The resulting deflection signal, which consists of the sum of k signals from the cantilever array, goes to an array of k phase-locked loops (PLLs) where each PLL locks to the unique resonant frequency of a single cantilever. Therefore there is a one-to-one pairing between cantilevers and PLLs. Each PLL determines its assigned cantilever's resonant frequency, by demodulating its deflection signal[26], then generates a sinusoidal drive signal at that frequency. The drive signals from each PLL are summed and used to drive a single piezoceramic actuator positioned directly underneath the chip, completing the feedback loop (**Supplementary Fig. 1**). Each PLL is configured such that it will track its cantilever's resonant frequency with a bandwidth of 50 or 100 Hz (Online Methods and **Supplementary Fig. 2**).

After acquiring the frequency signals for each cantilever, we convert them to mass units via each cantilever's sensitivity (Hz/pg), which must be known precisely. Although cantilever mass sensitivity should theoretically scale with the resonant frequency f to the power of 3/2 ($f^{3/2}$) (**Supplementary Note 2**), we found that the actual sensitivities occasionally deviated from the expected values and in some cases changed by up to 5% between days (**Supplementary Fig. 3**). To account for this, we measured the cantilever sensitivities during each experiment by spiking in inert monodisperse polystyrene–particle size standards into all samples. Because the particles are highly uniform (~1% coefficient of variation in diameter), we can easily distinguish them even when they are of similar size to the cells of interest.

The final step in extracting individual cell mass accumulation rates is to identify the frequency peaks in each cantilever that originate from the same cell. This is easily accomplished if the cells stay in the same order as they flow through the array. In practice, however, cells occasionally change order, divide or drop out of the queue (by adhering to a channel wall or getting physically stuck in the channel) and may re-enter the queue at a later time. To match frequency peaks to the cells that generated them, we use a probabilistic model based on our assumptions about the expected time for a cell to traverse a delay channel and about the fastest rates at which cells can change mass. We assume that mass accumulation rates are nearly constant on the timescale of our measurements, which constitute a small fraction of a cell cycle[16,17] (**Supplementary Note 3** and **Supplementary Fig. 4**). We then apply the Hungarian algorithm[27] to find a maximally likely way of matching all the cell events observed in cantilever 2 with the cells that have been observed in cantilever 1, followed by matching the cells observed in cantilever 3 with the cells observed in cantilevers 1 and 2, and so on. At concentrations used here, the matching is robust (better than 99% for simulated data; **Supplementary Fig. 5**), and can be manually verified for accuracy. At higher cell concentrations, the risk of incorrect matching increases, but outliers of interest can still be manually verified.

Device characterization

As these devices represent the first chips implementing SMR arrays, we asked whether operating 10–12 cantilevers simultaneously would decrease the performance of each cantilever. We measured the frequency noise for 12 large-channel cantilevers operating simultaneously using an optical-lever-based measurement system and observed minimal frequency noise (in terms of Allan deviations[28]) of 20–30 parts per billion at averaging times of 200–500 ms (**Supplementary Fig. 6**). Slightly lower Allan deviations were observed for small-channel devices (**Supplementary Fig. 6**), with optimal noise at shorter averaging times (30–100 ms). In both cases, these noise magnitudes are comparable to that routinely achieved with single-cantilever devices but have the potential to be further reduced—by an order of magnitude or more—before reaching thermomechanical limits (**Supplementary Fig. 6**).

To assess how well the devices could resolve a cell's mass accumulation rate, we first analyzed mixtures of polystyrene particles spanning 4–12 µm in diameter for large-channel devices and 1.0–2.5 µm

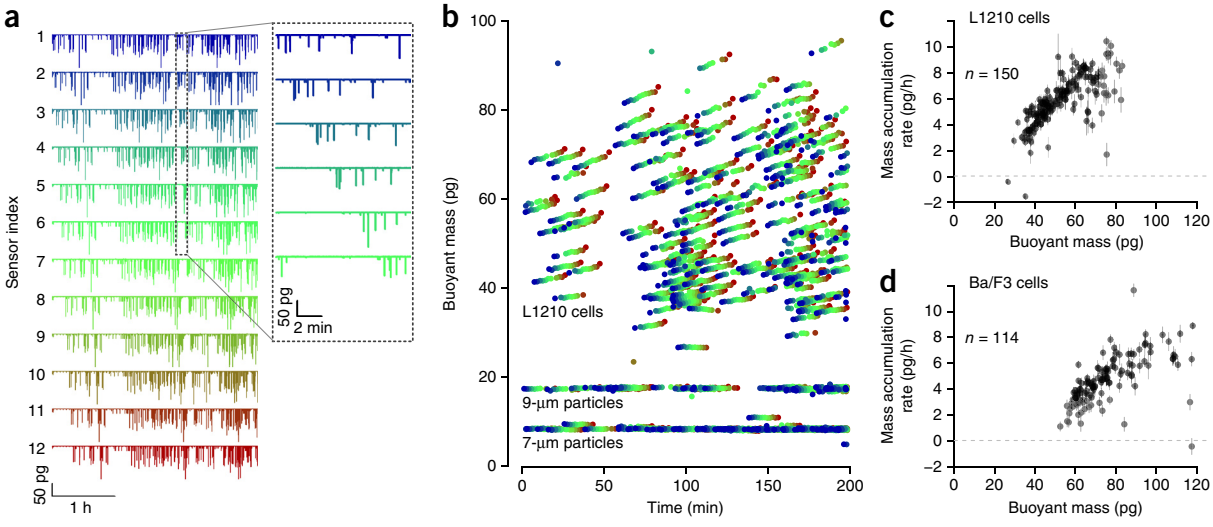

Figure 2 Measuring the growth of lymphoid cell lines. (**a**) Data from 12 cantilevers demonstrating continuous operation over roughly 3 h with L1210 cells at a flow rate of roughly 2 min between each cantilever (inset). (**b**) Buoyant mass data for L1210 cells extracted from frequency shifts of cantilevers; each color corresponds to a single cantilever, color-coded as in **a**. 7-µm particles were added as calibration; 9-µm particles were added as negative control (both are inert polystyrene particles). (**c**) Buoyant mass versus mass accumulation rate for L1210 cells in **b**, extracted via an automated peak-matching algorithm (**Supplementary Note 3**). Error bars indicate standard errors of the slope estimated directly from the fit. (**d**) Buoyant mass versus mass accumulation rate for Ba/F3 cells, showing a profile similar to that of L1210 cells but at larger cell sizes.

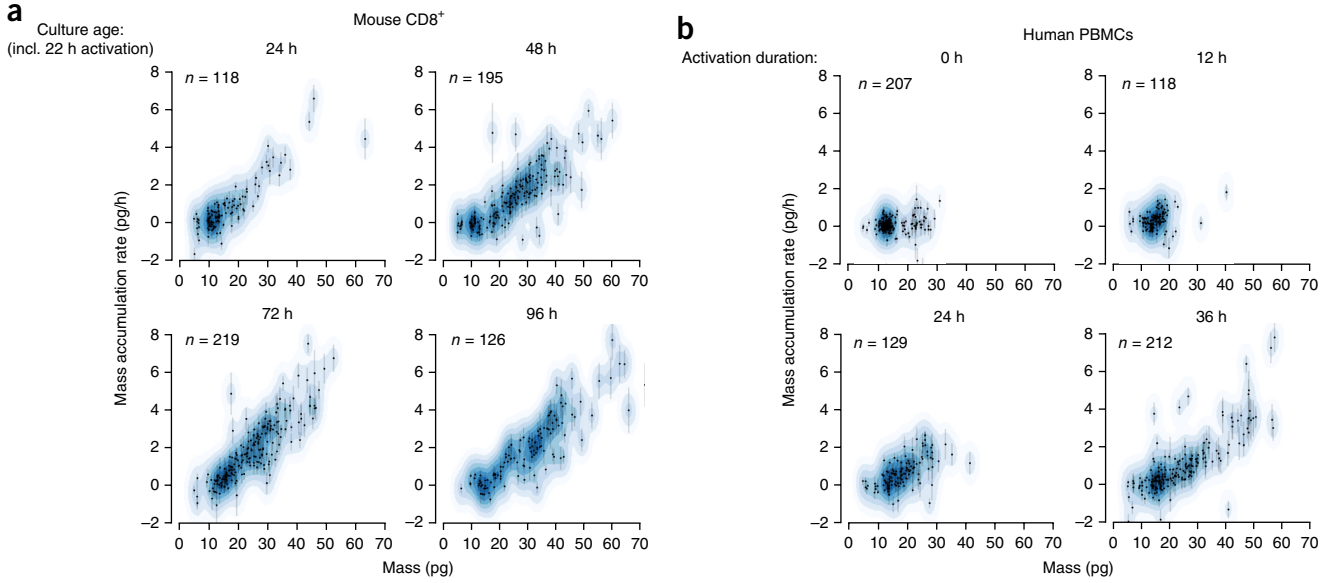

Figure 3 Measuring single immune-cell growth patterns and activation dynamics. (**a**) Mass accumulation rate over time in mouse CD8+ T cells activated with anti-CD3 and anti-CD28. Error bars indicate standard error of the slope, estimated directly from the regression fit. Points are overlaid on corresponding kernel density estimates (blue). (**b**) Lymphocyte activation, measured by quantifying mass and growth of single human PBMCs.

for small-channel devices. Our measurements clearly showed that these particles' masses were not changing, and the s.d. of the observed rates (an estimate for mass accumulation rate resolution) were 0.32 pg/h for the large-channel device (**Supplementary Fig. 7**) and 0.022 pg/h for the small-channel device (**Supplementary Fig. 8**). We also tested the large-channel device with fixed cells, which did not change in mass and showed a similarly low mass accumulation rate s.d. of 0.18 pg/h (**Supplementary Fig. 9**). These results are in agreement with what we would predict from equation (1) on the basis of the experimental flow rates and measured buoyant mass resolution.

Measuring growth rates of living cells

We used the large-channel serial SMR array to monitor the growth of steady-state L1210 cells (**Fig. 2**), a mouse lymphoblast cell line previously studied with SMRs[16,17]. In a 200-min experiment, we measured the size and mass accumulation rate of 150 cells. In the same time frame, a single SMR measuring each cell for 20 min could measure fewer than 10 cells, as it takes some time to switch between cells. As seen previously, these cells' mass accumulation rates were size-dependent and were higher for larger cells (**Fig. 2c**). We also measured Ba/F3 pro-B cells expressing the BCR–ABL oncoprotein. Under the same conditions as for the L1210 cells, we found a similar correlation

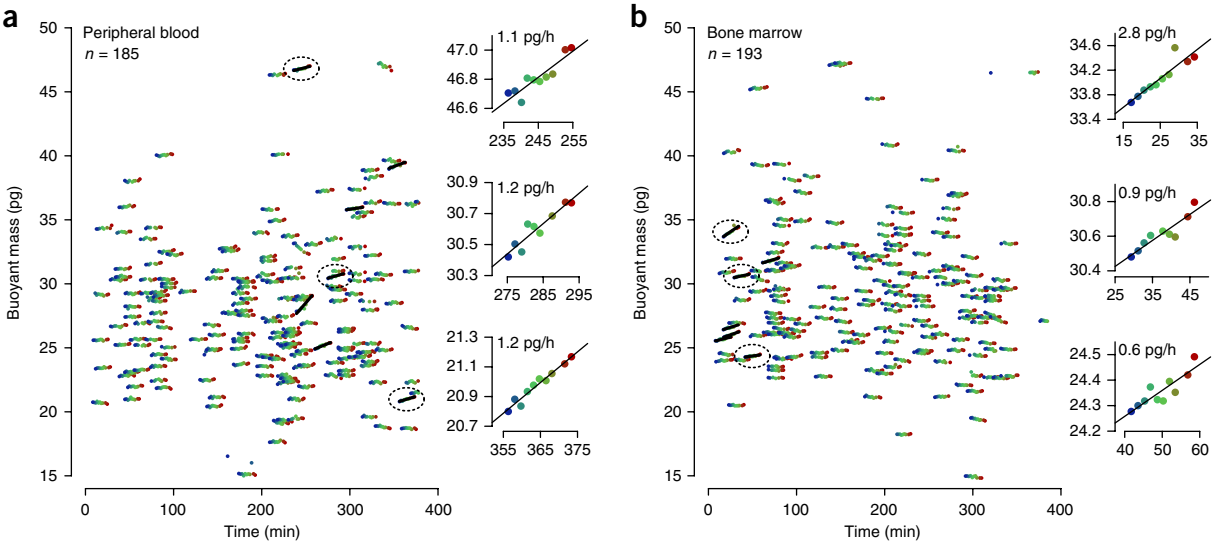

Figure 4 Measuring growth dynamics of single hCD15+hCD33+ AML cells from two patients. (**a**) Mass over time plotted for cells from a peripheral blood draw (**a**) or bone marrow (**b**). Cells with statistically significant growth ($P < 0.001$, one-sided t-test for slope > 0) are marked with black lines; insets show data for three growing cells. Not shown are 7-μm (~8.5 pg) particles included in these samples for calibration. Data from the first cantilever were not used in this analysis owing to abnormally high noise; **a** and **b** each reflect data from one (distinct) patient.

between mass and mass accumulation rate (**Fig. 2d**). As previously shown for L1210 cells[17] but not Ba/F3 cells, the mass accumulation rate per unit cell mass is lower for smaller cells compared to larger cells, suggesting that Ba/F3 cells also deviate from purely exponential growth in a manner similar to L1210s.

We next investigated whether we could measure primary cells, beginning with mouse CD8$^+$ T cells. CD8$^+$ T cells are known to drastically alter their metabolic activity and begin to grow in response to stimulation[29]. However, current methods for studying this transition often rely on bulk or single-time-point measurements, which makes it difficult to characterize heterogeneity in this phenotypic response over time. To this end, we activated mouse CD8$^+$ T cells *in vitro* and assayed their single-cell growth behavior daily for 4 d. Although the cumulative cell population grew robustly between daily measurements, the serial SMR consistently revealed a sizable nongrowing subpopulation (**Fig. 3a**) composed of the lowest-weight fractions (5–15 pg buoyant mass). Between 24 and 48 h, the growing subpopulation increased relative to the nongrowers and stayed roughly constant in size after 48 h. As with L1210 and Ba/F3 cells, although the mass accumulation rate covaried with size in all cases, it was not directly proportional to mass but was instead proportional to mass minus an offset. This departure from exponential growth is similar to that seen for the L1210 and Ba/F3 cells.

Our measurements of mouse CD8$^+$ T cells suggested we could rapidly assess human lymphocyte activation as an alternative to clinical techniques such as the lymphocyte transformation test[30,31]. This assay measures proliferation via DNA synthesis—typically via incorporation of tritiated thymidine—and requires several days to quantify bulk proliferation in response to activation. In contrast, we could directly observe activated lymphocytes within a population of unlabeled peripheral blood mononuclear cells (PBMCs) within 24–36 h after stimulation. We obtained PBMCs from whole blood, activated them for varying durations and then immediately measured their growth (**Fig. 3b**). Naive (t = 0 h) PBMCs show a clear subpopulation of cells between 20 and 30 pg, but this subpopulation was not detectable after 12 h of activation, consistent with monocyte adherence to the culture dish[32]. By 24 h, larger growing cells (putative activated T cells) were present, and by 36 h this population had expanded to even larger sizes and faster mass accumulation rates. The ability to assess growth within 36 h by mass accumulation of individual cells suggests the serial SMR array could provide a substantially faster method for assessing lymphocyte transformation than existing approaches that measure proliferation. Furthermore, quantitatively assessing single-cell growth within highly heterogeneous populations could help to identify responsive clones in a population of generally unresponsive cells. This functionality is particularly promising for fields such as cancer immunotherapy, where the characterization of rare, responsive lymphocytes may offer crucial insight for the identification of tumor neoantigens.

To further explore the capabilities of the system for studying primary cell growth kinetics, we asked whether we could detect growth in single putative cancer cells from patients. We enriched acute myeloid leukemia cells from the peripheral blood or bone marrow of two patients by flow sorting cells expressing human CD15 and CD33 (hCD15$^+$hCD33$^+$) (**Supplementary Fig. 10** and **Supplementary Table 1**), which were then maintained in serum-supplemented medium. In neither case was the tumor immunophenotype known in advance, so the collected cell populations were heterogeneous owing to the conservative sorting strategy. Although no growth was visible at the population level over the first 48 h (**Supplementary Fig. 11**), we detected a rare subpopulation of cells (~4% of each sample)

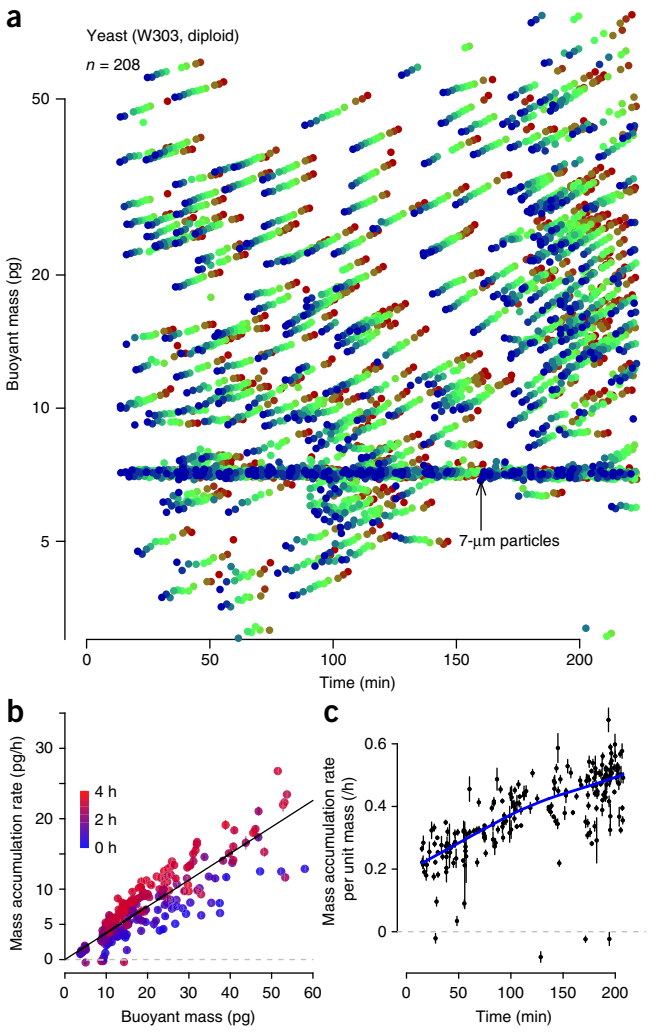

Figure 5 Measuring lag-phase yeast culture time-resolved growth dynamics at single-cell resolution. (**a**) Semilog plot of buoyant mass trajectories of yeast cells in rich medium. Data from SMR 9 were not used owing to very high noise. Particles between 5 and 20 pg are probably mostly single cells; particles with mass >20 pg are mostly clumps of cells. (**b**) Buoyant mass versus mass accumulation rate. Error bars indicate standard error of the slope estimated from each regression of buoyant mass versus time. (**c**) Mass accumulation rate per unit mass (interpretable as exponential growth rate) versus time. Error bars indicate standard error of the slope divided by the cell's buoyant mass. Blue line shows locally weighted scatterplot smoothing (LOWESS) curve.

that were accumulating mass when we analyzed these samples on the serial SMR array 3–9 h after sample acquisition (**Fig. 4**). These cells typically grew between 0.2 and 1 pg over the 20-min measurement, which would correspond to a <1% change in diameter. We also noted another rare subpopulation of cells losing mass, which may be in the process of dying. These data—though exploratory—show that the serial SMR can resolve heterogeneous growth patterns in primary patient samples.

We next investigated whether the large-channel serial SMR array could be used to study *S. cerevisiae,* a model organism of interest in studies of growth-rate control and size homeostasis[3,13]. We measured the growth of single yeast cells in lag phase—a brief period of slow or no growth after transfer from spent medium to fresh medium. In a 3.5-h experiment, we measured the mass accumulation rates of

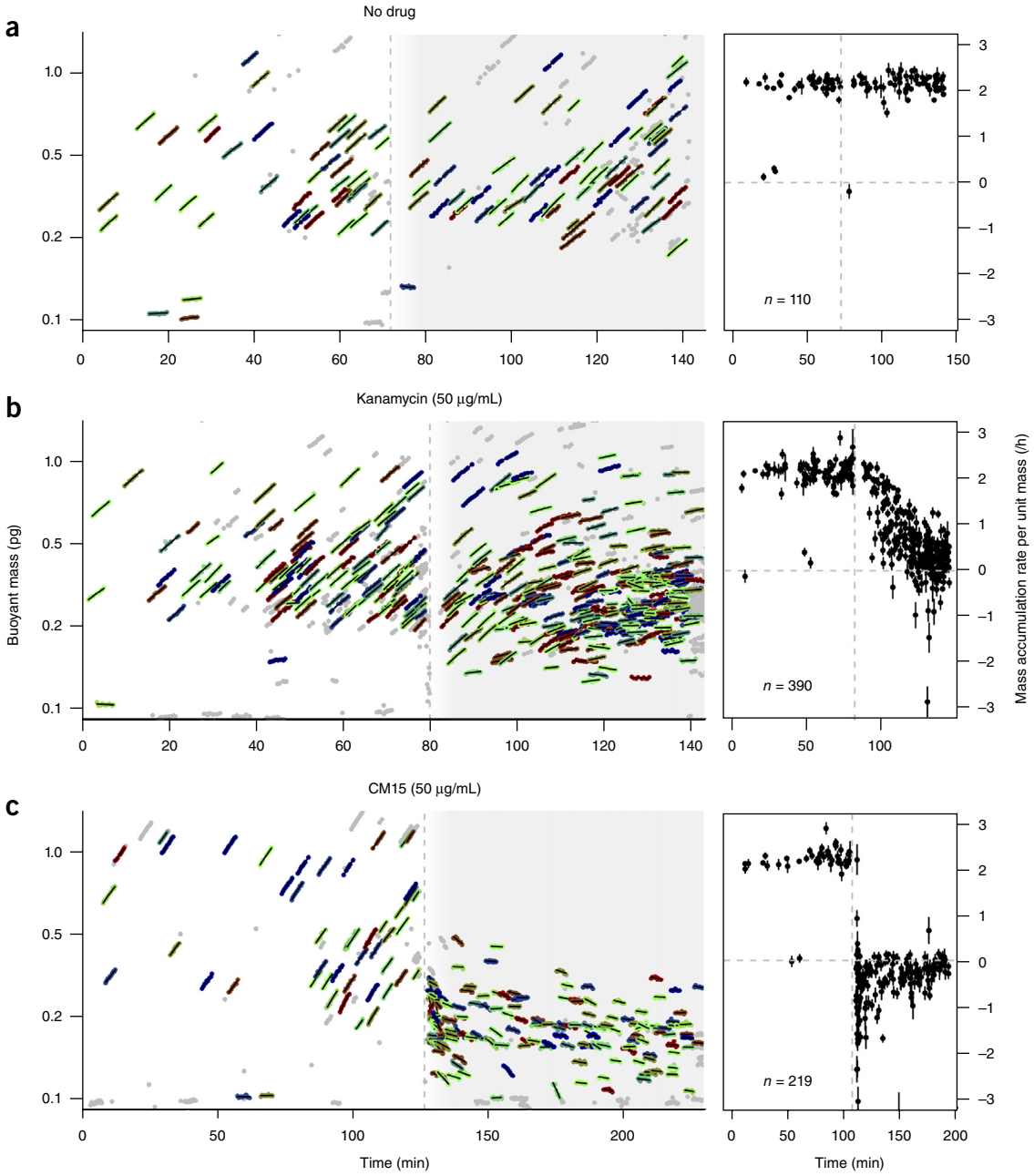

Figure 6 Measuring bacterial growth and drug response on a small-channel serial SMR array. (**a**–**c**) Serial SMR array buoyant mass measurements (left) and plots of mass accumulation rate per unit mass versus time (right) for *E. coli* cultures without drug (**a**) or in the presence of kanamycin (**b**) or CM15 (**c**). Colored dots with overlaid lines (left) indicate cells included in the analysis at right; gray dots indicate data for which <6 mass measurements could be linked together or the automated matching was uncertain. Data from polystyrene particles used for calibration were omitted for clarity. Error bars indicate standard errors of regression parameter for normalized growth rate. Vertical dashed lines indicate the time at which a drug was added (**b**,**c**).

208 cells (or cell clumps, as daughter cells often remain adhered to mother cells after division) (**Fig. 5**). We plotted these cells' masses on a logarithmic scale because single yeast cells grow exponentially[3,16]. On a semilog plot the slope of a cell's mass trajectory may be interpreted as an exponential growth rate, which is equivalent to its mass accumulation rate per unit mass. Below we refer to this as the cell's growth rate. Throughout the first several hours following inoculation into fresh medium, the cell growth rates increased toward their maximal rate of approximately 0.5 per hour (**Fig. 5b**,**c**). Notably, the initial growth rate (i.e., immediately after inoculation into fresh medium) was not 0 but rather around 0.2/h, showing that yeast in stationary phase remain primed to begin growing immediately, albeit at a submaximal rate, should conditions become favorable.

We next asked whether serial SMR arrays designed for bacteria could provide rapid and precise measurements of bacterial growth. We first investigated the growth of single log-phase *E. coli* cells (**Fig. 6a**). In rich medium (LB) at 37 °C, the average growth rate of individual bacteria was 2.14 ± 0.02/h (mean ± s.e.m., 19.4 min doubling time) with a coefficient of variation of 7.4% excluding four outlying small cells (**Fig. 6a**), in good agreement with other recent measurements[12].

However, it is notable that we were measuring growth on a much shorter timescale (4 min instead of a full 20-min cell cycle) and that the biological variation on this timescale was no larger than at longer timescales. We were also able to measure growth of the Gram-positive coccus *E. faecalis* (**Supplementary Fig. 12**). This strain behaved similarly to the Gram-negative rod *E. coli* in the serial SMR array, growing at easily detectable rates with a mean of 1.86 ± 0.02/h. The serial SMR array can thus provide high-resolution and rapid growth measurements of single Gram-positive and Gram-negative bacteria of varying morphologies, including clinically relevant species.

We next asked whether we could observe the effects of antibiotics on bacterial growth. We added kanamycin to an *E. coli* culture midway through the experiment (**Fig. 6b**), after which the growth rate dropped rapidly, reaching almost 0 in less than 0.5 h. This result demonstrates the potential for assessment of antibiotic susceptibility and quantification of killing kinetics on an unprecedented timescale. Furthermore, we noted variation in the timescale of growth arrest: after 20 min of exposure to kanamycin, some cells had nearly stopped growing while others continued growing near their maximal rate.

Finally, we asked whether we could observe the growth-arresting effects of the antimicrobial peptide CM15 (ref. 33), which is known to permeabilize cells on short timescales but does not change the overall cell size as measured by microscopy[34]. When we added CM15 to the *E. coli* culture, we observed an immediate decrease in mean cell mass and an immediate cessation of mass accumulation (**Fig. 6c**). Although most cells appeared to be neither growing nor decreasing in mass, we observed rapid loss of mass in several cells immediately after peptide addition and up to nearly 1 h later.

DISCUSSION

We have shown that the serial SMR array can precisely measure single-cell mass accumulation rates for up to 60 mammalian or 150 bacterial cells per hour. This enables observation of the full distribution of growth behaviors—including rare cells behaving very differently from the average cell—on short timescales. This method is compatible with a variety of cell types, including cell lines, primary blood cells, yeast and bacteria, and can be used to profile the response of cells in culture to perturbations, including small-molecule therapeutics and peptides. We envision that this device will be applicable in many areas of research and potentially in a clinical setting. The ability to detect rare growing cells in complex mixtures from patients suggests the possibility of correlating these types of measurements to disease states and assessing drug susceptibility in these rare cells. Outside of medical applications, the serial SMR system could be used to quantify cellular heterogeneity to determine how cell growth is intrinsically tied to a broad array of molecular-scale phenomena.

Our system has both benefits and drawbacks compared to microscopy, which has long been a mainstay for studying cell growth. Small-channel serial SMR arrays provide at least tenfold higher precision than that reported in a recent quantitative phase microscopy study[35] (**Supplementary Note 4** and **Supplementary Fig. 13**). Furthermore, at slower flow rates, the precision increases by another two- to threefold, to a level achievable with dynamic trapping measurements performed on a single SMR (**Supplementary Fig. 13**). This higher resolution is probably the reason we observed substantially less cell-to-cell variability (**Supplementary Fig. 13b**,**d**). The high precision applies to cells in flow, including motile cells, which is advantageous for automated clinical assays such as antibiotic-susceptibility testing; however, there are drawbacks to our method. The serial SMR array is currently not suitable for measuring growth of cells that are attached to a surface. Furthermore, unlike microscopy, this method can capture only short 'snapshots' of single-cell growth, though the length of the snapshot may increase in the future with increasing SMR parallelization. Finally, microscopes are more widely available and easier to operate than the current version of our serial SMR system.

In future work, the serial SMR approach described here could be optimized further. Improving the actuation and detection schemes might reasonably enable an order-of-magnitude improvement in mass accumulation rate precision (**Supplementary Fig. 6**), and this extra precision could be exchanged directly for higher throughput by increasing the flow rates of cells transiting the array (**Supplementary Note 1** and **Supplementary Fig. 14**). Another possibility is to further parallelize the system by implementing many serial SMR arrays on a single chip, enabling measurement of cells under many conditions simultaneously—for example, bacteria in several different concentrations of antibiotic. Other future advancements could include integration with fluorescence microscopy and methods to sort cells on the basis of growth rate, both of which would greatly expand the potential for correlative assays that link growth kinetics with underlying biology.

METHODS

Methods and any associated references are available in the online version of the paper.

Note: Any Supplementary Information and Source Data files are available in the online version of the paper.

ACKNOWLEDGMENTS

We thank G. Szeto for providing mouse spleen and lymph nodes, J.H. Kang for measuring the density of RPMI 1640 and A. Amon for a critical reading of the manuscript. This work was carried out in part through the use of the Microsystems Technology Laboratories at the Massachusetts Institute of Technology (MIT). Support was provided by the Bridge Project (a partnership between the Koch Institute for Integrative Cancer Research at MIT and the Dana-Farber/Harvard Cancer Center) to S.R.M. and D.M.W.; the US Army Research Office (Institute for Collaborative Biotechnologies grant W911NF-09-D-0001) to S.R.M.; the US National Science Foundation (1129359) to S.R.M.; Institut Mérieux to S.R.M.; and the US National Cancer Institute (Physical Sciences Oncology Center U54CA143874 and Cancer Center Support grants P30-CA14051 and R33-CA191143) to S.R.M. N.C. acknowledges support from an MIT Poitras Fellowship. M.A.M. acknowledges support from NCI institutional research training grant T32 CA009172, awarded to the Department of Medical Oncology at Dana-Farber Cancer Institute. M.M.S. acknowledges support from the NIH/NIGMS T32 GM008334 Interdepartmental Biotechnology Training Program grant. D.M.W. is a Leukemia and Lymphoma Society Scholar.

AUTHOR CONTRIBUTIONS

N.C., S.O. and F.F.D. designed devices; N.C., S.O. and S.C.W. designed and constructed the experimental setup; K.R.P., M.O., V.A. and F.B. fabricated the devices; N.C., S.O., M.M.S., R.J.K., S.M.K., A.S., Y.K., D.M.W. and S.R.M. designed the experiments, N.C., S.O., S.M.K., R.J.K., M.A.M. and M.M.S. performed the experiments; N.C. analyzed the data; N.C., S.O. and S.R.M. wrote the paper with input from all authors.

COMPETING FINANCIAL INTERESTS

The authors declare competing financial interests: details are available in the online version of the paper.

1. Labhsetwar, P., Cole, J.A., Roberts, E., Price, N.D. & Luthey-Schulten, Z.A. Heterogeneity in protein expression induces metabolic variability in a modeled *Escherichia coli* population. *Proc. Natl. Acad. Sci. USA* **110**, 14006–14011 (2013).
2. Balaban, N.Q., Merrin, J., Chait, R., Kowalik, L. & Leibler, S. Bacterial persistence as a phenotypic switch. *Science* **305**, 1622–1625 (2004).
3. Di Talia, S., Skotheim, J.M., Bean, J.M., Siggia, E.D. & Cross, F.R. The effects of molecular noise and size control on variability in the budding yeast cell cycle. *Nature* **448**, 947–951 (2007).
4. van Heerden, J.H. *et al.* Lost in transition: start-up of glycolysis yields subpopulations of nongrowing cells. *Science* **343**, 1245114 (2014).

5. Sandler, O. *et al.* Lineage correlations of single cell division time as a probe of cell-cycle dynamics. *Nature* **519**, 468–471 (2015).
6. Reya, T., Morrison, S.J., Clarke, M.F. & Weissman, I.L. Stem cells, cancer, and cancer stem cells. *Nature* **414**, 105–111 (2001).
7. Keren, I., Kaldalu, N., Spoering, A., Wang, Y. & Lewis, K. Persister cells and tolerance to antimicrobials. *FEMS Microbiol. Lett.* **230**, 13–18 (2004).
8. Fridman, O., Goldberg, A., Ronin, I., Shoresh, N. & Balaban, N.Q. Optimization of lag time underlies antibiotic tolerance in evolved bacterial populations. *Nature* **513**, 418–421 (2014).
9. Aldridge, B.B. *et al.* Asymmetry and aging of mycobacterial cells lead to variable growth and antibiotic susceptibility. *Science* **335**, 100–104 (2012).
10. Wang, P. *et al.* Robust growth of *Escherichia coli*. *Curr. Biol.* **20**, 1099–1103 (2010).
11. Moffitt, J.R., Lee, J.B. & Cluzel, P. The single-cell chemostat: an agarose-based, microfluidic device for high-throughput, single-cell studies of bacteria and bacterial communities. *Lab Chip* **12**, 1487–1494 (2012).
12. Taheri-Araghi, S. *et al.* Cell-size control and homeostasis in bacteria. *Curr. Biol.* **25**, 385–391 (2015).
13. Ferrezuelo, F. *et al.* The critical size is set at a single-cell level by growth rate to attain homeostasis and adaptation. *Nat. Commun.* **3**, 1012 (2012).
14. Barer, R. Interference microscopy and mass determination. *Nature* **169**, 366–367 (1952).
15. Zangle, T.A. & Teitell, M.A. Live-cell mass profiling: an emerging approach in quantitative biophysics. *Nat. Methods* **11**, 1221–1228 (2014).
16. Godin, M. *et al.* Using buoyant mass to measure the growth of single cells. *Nat. Methods* **7**, 387–390 (2010).
17. Son, S. *et al.* Direct observation of mammalian cell growth and size regulation. *Nat. Methods* **9**, 910–912 (2012).
18. Park, K. *et al.* Measurement of adherent cell mass and growth. *Proc. Natl. Acad. Sci. USA* **107**, 20691–20696 (2010).
19. Burg, T.P. *et al.* Vacuum-packaged suspended microchannel resonant mass sensor for biomolecular detection. *J. Microelectromech. Syst.* **15**, 1466–1476 (2006).
20. Feijó Delgado, F. *et al.* Intracellular water exchange for measuring the dry mass, water mass and changes in chemical composition of living cells. *PLoS One* **8**, e67590 (2013).
21. Lee, J., Bryan, A.K. & Manalis, S.R. High precision particle mass sensing using microchannel resonators in the second vibration mode. *Rev. Sci. Instrum.* **82**, 023704 (2011).
22. Lee, J. *et al.* Suspended microchannel resonators with piezoresistive sensors. *Lab Chip* **11**, 645–651 (2011).
23. Lee, J., Shen, W., Payer, K., Burg, T.P. & Manalis, S.R. Toward attogram mass measurements in solution with suspended nanochannel resonators. *Nano Lett.* **10**, 2537–2542 (2010).
24. Carson, J.R. Notes on the theory of modulation. *Proc. Inst. Radio Eng.* **10**, 57–64 (1922).
25. Tortonese, M., Yamada, H., Barrett, R.C. & Quate, C.F. Atomic force microscopy using a piezoresistive cantilever. *Transducers* **1991**, 448–451 (1991).
26. Olcum, S., Cermak, N., Wasserman, S.C. & Manalis, S.R. High-speed multiple-mode mass-sensing resolves dynamic nanoscale mass distributions. *Nat. Commun.* **6**, 7070 (2015).
27. Kuhn, H.W. The Hungarian method for the assignment problem. *Nav. Res. Logist. Q.* **2**, 83–97 (1955).
28. Allan, D.W. Statistics of atomic frequency standards. *Proc. IEEE* **54**, 221–230 (1966).
29. Fox, C.J., Hammerman, P.S. & Thompson, C.B. Fuel feeds function: 934energy metabolism and the T-cell response. *Nat. Rev. Immunol.* **5**, 844–852 (2005).
30. Halpern, B. & Amache, N. Diagnosis of drug allergy in vitro with the lymphocyte transformation test. *J. Allergy* **40**, 168–181 (1967).
31. Poujol, F. *et al.* Flow cytometric evaluation of lymphocyte transformation test based on 5-ethynyl-2′deoxyuridine incorporation as a clinical alternative to tritiated thymidine uptake measurement. *J. Immunol. Methods* **415**, 71–79 (2014).
32. Elkord, E., Williams, P.E., Kynaston, H. & Rowbottom, A.W. Human monocyte isolation methods influence cytokine production from *in vitro*–generated dendritic cells. *Immunology* **114**, 204–212 (2005).
33. Andreu, D. *et al.* Shortened cecropin A-melittin hybrids. Significant size reduction retains potent antibiotic activity. *FEBS Lett.* **296**, 190–194 (1992).
34. Fantner, G.E., Barbero, R.J., Gray, D.S. & Belcher, A.M. Kinetics of antimicrobial peptide activity measured on individual bacterial cells using high-speed atomic force microscopy. *Nat. Nanotechnol.* **5**, 280–285 (2010).
35. Mir, M. *et al.* Optical measurement of cycle-dependent cell growth. *Proc. Natl. Acad. Sci. USA* **108**, 13124–13129 (2011).

ONLINE METHODS

Device design and fabrication. Devices were fabricated using previously described methods[22,36]. Large-channel devices used with optical-lever readout were fabricated at MIT's Microsystems Technology Laboratories and Innovative Micro Technology (IMT), and large-channel devices with embedded piezoresistors for readout were fabricated at CEA–LETI. Notably, the large devices designed for optical-lever readout did not include a getter layer, but the cavity surrounding the cantilevers remained in vacuum. Large-channel devices had cantilever interior channels of 15 × 20 μm in cross-section, and delay channels 20 × 30 μm in cross-section. Only human PBMC measurements were carried out on large-channel devices fabricated at CEA–LETI; all other mammalian cell and yeast experiments were on devices fabricated at IMT without piezoresistors. Small-channel devices were fabricated at IMT and had cantilever channels 3 × 5 μm in cross-section, and delay channels 4 × 15 μm in cross-section. The tips of the cantilevers in the array are aligned (**Fig. 1**) so that a single line-shaped laser beam can be used for optical-lever readout (**Supplementary Fig. 1**). The cantilevers were arrayed such that the shortest (and therefore most sensitive) cantilevers were at the ends of the array. Before use, the device was first cleaned with piranha (3:1 sulfuric acid to 50% hydrogen peroxide) and the channel walls were passivated with polyethylene glycol (PEG) grafted onto poly-L-lysine (SuSoS).

System setup. A full schematic and picture for the device setup using optical-lever based detection is shown in **Supplementary Figure 1**. A piezoceramic actuator seated underneath the device is used for actuation. The custom-made low-noise photodetector, Wheatstone bridge–based amplifier (for piezoresistor readout) and high-current piezoceramic driver have been described elsewhere[37]. It is worth noting that in previous readout systems designed for a single cantilever, signal distortion (via electronic saturation or optical interference patterns) did not typically contribute to system noise, as the distortion generates spectral components at integer multiples of the carrier frequency that are easily filtered out. However, in a channel carrying many signals, nonlinear distortion (especially saturation) will generate noise near the carrier signals (**Supplementary Fig. 15**). Therefore, care must be taken to ensure that no signals become saturated. To avoid the effects of optical interference between signals from different cantilevers (producing harmonics at the difference frequency), we used a low-coherence-length light source (675 nm superluminescent diode, 7 nm full-width half-maximum spectral width, Superlum) for our optical lever. After the custom photodetector converts the optical signal to a voltage signal, the voltage signal is fed into a field-programmable gate array (FPGA) board, for which implementation details were published previously[26]. Briefly, the FPGA implements 12 parallel second-order phase-locked loops that both demodulate and drive a single cantilever. The FPGA is a Cyclone IV FPGA (Altera) on a DE2-115 development board (Terasic Inc.) operating on a 100 MHz clock (AOCJY2 oven-controlled crystal oscillator, Abracon). Analog input and output were via a high-speed analog-to-digital/digital-to-analog (AD/DA) card (DCC HSMC card, Terasic Inc.) operating 14-bit AD and DA converters at 100 MHz.

System operation. To operate all cantilevers in the array, we first measure the resonator array transfer function by sweeping the driving frequency and recording the amplitude and phase of the array response. We next calculate parameters for each PLL such that each cantilever-PLL feedback loop has a 50- or 100-Hz FM-signal bandwidth. We then adjust the phase-delay for each PLL to maximize the cantilever vibration amplitude. Finally, we measure the FM-signal transfer function for each cantilever–PLL feedback loop to confirm sufficient measurement bandwidth (in case of errors in setting the parameters). This transfer function relates the measured cantilever–PLL oscillation frequency to a cantilever's time-dependent intrinsic resonant frequency. Frequency data for each cantilever are collected at 500 Hz, and are transmitted from the FPGA via Ethernet to a personal computer where they are saved via custom LabView software (National Instruments).

As in previous SMR systems, the device is placed on a copper heat sink/source connected to a heated water bath maintained at 30 °C (yeast) or 37 °C (mammalian cells and *E. coli*) for the duration of the experiment. The sample is loaded into the device from vials pressurized under air (yeast and *E. coli*) or air with 5% CO_2 (mammalian cells) (**Supplementary Fig. 1**), through 0.009-inch inner-diameter fluorinated ethylene propylene (FEP) tubing. The pressurized vials are seated in a temperature-controlled sample holder throughout the measurement. FEP tubing allows us to flush the device with piranha solution for cleaning, as piranha will damage most nonfluorinated plastics. To measure a sample of cells, we first flush the device with filtered medium and then flush the sample into one bypass channel. NIST-traceable polystyrene beads are added to the sample as an internal calibration standard. For experiments on large-channel devices, we typically apply between 1 and 2 p.s.i. across the entire array, yielding flow rates on the order of 0.5 nL/s (the array's calculated fluidic resistance is approximately 3×10^{16} Pa/(m^3/s), calculated as described[38]). For small-channel devices, we apply 4–5 p.s.i. across the array, yielding flow rates of ~0.1 nL/s. Additionally, every several minutes we flush new sample into the input bypass channel to prevent particles and cells from settling in the tubing and device. Between experiments, devices are cleaned with filtered 2% tergazyme, filtered 10% bleach or piranha solution.

Data analysis. We first rescale the recorded frequency signals from each cantilever by applying a rough correction for the different sensitivities of the cantilevers. Cantilevers differing only in length should have mass sensitivities proportional to $f^{3/2}$. Therefore we initially divide each frequency signal by its carrier frequency to the power of 3/2 such that the signals are of similar magnitude. To detect peaks, we filter the data with a third-order Savitzky–Golay low-pass filter[39] followed by a nonlinear high-pass filter (subtracting the results of a moving quantile filter from the data). We find peak locations as local minima that occur below a user-defined threshold. After finding the peak locations, we estimate the peak heights by fitting the surrounding baseline signal (to account for a possible slope in the baseline that was not rejected by the high-pass filter), fitting the region surrounding the local minima with a fourth-order polynomial and finding the maximum difference between the predicted baseline and the local minima polynomial fit. Because this process occasionally makes errors (it sometimes detects noise, particles that got stuck in the cantilever and particles that passed through the cantilever at the same time), for each cantilever we reject peaks that are very unlike the typical peak. We do this by first calculating the robust Mahalanobis distance for each peak in terms of a number of its estimated characteristics (baseline slope, time between sequential antinode peaks, minimum value between sequential peaks and difference in heights of sequential peaks) and rejecting those with large distances above a user-specified threshold, then identifying the peaks corresponding to the calibration particles and precisely estimating the mass sensitivity for each cantilever such that the modal mass for the particles is equal to the expected modal mass according to the manufacturer's data sheet. Finally we match up peaks at different cantilevers that originate from the same cell to extract single-cell growth information (**Supplementary Note 3**). **Figures 2–5** show the mass accumulation rates of automatically matched cells that were observed at least seven times. For *E. coli* (**Fig. 6**), because the cell concentrations were higher, we required both that the cell was measured at least six out of ten times and that the r.m.s. error of a linear fit (buoyant mass versus time) was less than 5 fg, as a greater fitting error suggests a possibly incorrect matching.

Cell culture. *E. coli* strain 25922 (ATCC) was grown overnight in LB medium (Miller, Difco) at 37 °C. Saturated overnight cultures were diluted 10,000-fold in LB supplemented with 0.2% Tween-80 (to prevent particles from sticking to the device walls) and incubated 1.5–2.5 h in a shaker incubator at 37 °C before being loaded onto the serial SMR array. The CM15 peptide (sequence KWKLFKKIGAVLKVL; Biosynthesis) was ordered as a crude synthesis and suspended in water by weight. Kanamycin (Sigma-Aldrich) and CM15 were prepared as stock solutions at 50 mg/mL in water, and 1 μL of stock solution was added to 1 mL culture at the times indicated.

E. faecalis (ATCC strain 29212) was grown overnight in Brain Heart Infusion medium (BHI, Difco) at 37 °C. Saturated overnight cultures were diluted 100,000-fold in BHI with 0.2% Tween-80 and incubated for 3 h in a shaker incubator at 37 °C before being loaded onto the serial SMR array.

Yeast (strain W303, diploid) were a gift from A. Amon and were maintained on YPD agar plates and grown in YPD broth at 30 °C.

L1210 cells were a gift from M. Kirschner, and no further cell-line validation was performed. Ba/F3 cells expressing BCR and ABL were created[40] from the parental Ba/F3 cell line obtained from the RIKEN BioResource Center.

doi:10.1038/nbt.3666

Both cell lines tested negative for mycoplasma. L1210 and Ba/F3 cells were cultured in filtered RPMI 1640 supplemented with 10% FBS and streptomycin and penicillin at 37 °C under 5% CO_2. Ba/F3 cells were cultured under identical conditions and were IL-3 independent owing to a BCR–ABL insertion.

Mouse $CD8^+$ T cells were obtained from a 14-week-old female C57BL/6J mouse. Animals were cared for in accordance with federal, state, and local guidelines following a protocol approved by the Department of Comparative Medicine (DCM) at MIT. Cells were obtained from a mouse spleen and two lymph nodes, ground through a filter, subjected to ammonium–chloride–potassium (ACK) lysis, purified with a $CD8a^+$ T Cell Isolation Kit (Miltenyi) and immediately seeded into wells and activated in RPMI 1640 with 10% FBS, 1× streptomycin–penicillin, and 55 μM β-mercaptoethanol (Gibco) using surface-bound anti-CD3 (BioLegend 145-2C11, coated at 5 μg/mL) and soluble anti-CD28 (BioLegend, 37.51, 2 μg/mL) at 37 °C under 5% CO_2 for 22 h. After 22 h, cells were transferred to new medium containing IL-2 (100 U/mL) and from then on were passaged daily to a concentration of roughly 200,000 cells/mL 2–3 h before each measurement.

Human blood buffy coat was obtained from Research Blood Components, and PBMCs were isolated with Ficoll-Paque Plus (GE) using the manufacturer's recommended protocol. The PBMC layer was isolated, subjected to ACK lysis (Thermo Fisher) and washed three times with RPMI 1640 supplemented with 10% FBS. Cells were then seeded in a 96-well plate (Corning High Bind microplate) at a concentration of 1.5×10^6 mL^{-1} with 5 μg/mL surface-bound anti-CD3 (BioLegend, HIT3a clone), 2 μg/mL soluble anti-CD28 (BioLegend, CD28.2 clone), and 100 U/mL soluble IL-2 (PeproTech) at 37 °C under 5% CO_2. Immediately before measurement, cells were harvested from the well by gentle pipetting to suspend weakly adhered cells, diluted into RPMI 1640 supplemented with 10% FBS and IL-2 and loaded into the serial SMR array.

All studies involving primary patient samples were approved by the Dana-Farber/Harvard Cancer Center Institutional Review Board. Informed consent was obtained in accordance with the Declaration of Helsinki. Diagnostic peripheral blood or bone marrow specimens were obtained from patients with acute myeloid leukemia (**Supplementary Table 1**), subject to erythrocyte lysis (Qiagen, #158904), and stained with antibodies targeting hCD45 (eBiosciences, #17-9459-42) and hCD15 (eBiosciences, #12-0159-42). Leukemia cells were enriched by sorting for $hCD45^+hCD15^+$ (double-positive) cells on a FACSAria II SORP fluorescence activated cell sorter (BD Biosciences) (**Supplementary Fig. 8**). Sorted cells were seeded at a density of 1×10^6 cells/mL and cultured at 37 °C in a humidified 5% CO_2 incubator in RPMI (Gibco) supplemented with 10% FCS (Gibco), 2 mM L-glutamine (Gibco), and 50 IU/ml–50 μg/mL penicillin–streptomycin (Fisher Scientific) before dilution and loading on the SMR.

36. Burg, T.P. *et al.* Weighing of biomolecules, single cells and single nanoparticles in fluid. *Nature* **446**, 1066–1069 (2007).
37. Olcum, S. *et al.* Weighing nanoparticles in solution at the attogram scale. *Proc. Natl. Acad. Sci. USA* **111**, 1310–1315 (2014).
38. Stone, H.A. in *CMOS Biotechnology* (eds. Lee, H., Westervelt, R.M. & Ham, D.) 5–30 (Springer US, 2007).
39. Savitzky, A. & Golay, M.J.E. Smoothing and differentiation of data by simplified least squares procedures. *Anal. Chem.* **36**, 1627–1639 (1964).
40. Lane, A.A. *et al.* Triplication of a 21q22 region contributes to B cell transformation through HMGN1 overexpression and loss of histone H3 Lys27 trimethylation. *Nat. Genet.* **46**, 618–623 (2014).